




Dielectric control of ultralight hollow porous carbon spheres and excellent microwave absorbing properties

Digang Fan^{1,*} , Bo Wei², Ruixin Wu¹, Jintang Zhou², and Congyu Zhou²

¹School of Electronic Science and Engineering, Nanjing University, Nanjing 210023, China

²College of Materials and Technology, Nanjing University of Aeronautics and Astronautics, Nanjing 211100, China

Received: 24 August 2020

Accepted: 4 January 2021

Published online:

15 January 2021

© The Author(s), under exclusive licence to Springer Science+Business Media, LLC part of Springer Nature 2021

ABSTRACT

Carbon materials have the potential to be excellent absorbing materials due to their lighter weight, easy-to-control graphitization degree and good dielectric properties. However, a single carbon material is often difficult to achieve the ideal electromagnetic wave attenuation effect due to the imbalance of impedance matching and the lack of magnetic loss. In this work, a simple sol-gel method was used to control the hydrolysis reaction of tetraethyl orthosilicate and the synthesis reaction of phenolic resin to prepare the core-shell precursor of silica coated with phenolic resin/silica spheres. After high-temperature calcination and pickling etching, hollow carbon spheres (HPC) with porous structure were obtained. By adjusting the calcination temperature, the crystallinity and dielectric properties of HPC can be easily adjusted. With an ultra-low filling ratio of 5 wt%, HPC can obtain a wide-band effective microwave absorbing performance of 5.73 GHz (2–18 GHz band) under an ultra-thin thickness of 2.0 mm, which is an excellent absorbing agent with lightweight, thin thickness, strong absorbing ability and wide absorbing band. Considering the simple preparation scheme, HPC is expected to become one of the candidates for high-efficiency microwave absorbers. The special hollow, porous structure and suitable degree of graphitization are the main reasons for the effective wave absorption of HPC.

Introduction

With the rapid development of electromagnetic technology, the negative impact of electromagnetic interference (EMI) on human production and life is

also increasing [1–3]. Electromagnetic wave-absorbing material (EAM) is considered to be an effective way to solve the EMI problem because it can convert electromagnetic wave energy into heat energy loss through relaxation, resonance, etc., and thus significantly absorb the incoming

Handling Editor: Dale Huber.

Address correspondence to E-mail: Digang_fan@163.com

electromagnetic wave energy [4, 5]. Excellent EAM needs to achieve effective absorption of electromagnetic waves (broadband, strong absorption) at a low filling rate to meet the requirements of lightweight and low density for modern applications. However, traditional magnetic EAM, such as ferrite and ultra-fine metal powder, can only achieve better absorbing effects at a higher filling rate [6–8]. The large proportion greatly affects its application in the field of wave absorption. In contrast, carbon materials have the advantages of low density, good chemical stability and good corrosion resistance. At the same time, they can obtain good wave absorbing ability through strong interference under thinner thickness. In addition, its dielectric properties are directly affected by the degree of graphitization of the carbon material itself, and the degree of graphitization can be easily adjusted by controlling the crystallization temperature to achieve the purpose of adjusting the dielectric properties [9]. Therefore, carbon materials are undoubtedly one of the candidates for excellent EAM.

Traditional carbon-based EAMs such as graphite, carbon black and carbon fiber have been proven to have good absorbing ability due to their large dielectric loss factor ($\tan \delta_e$) [10, 11]. However, a single dielectric property often leads to an imbalance in impedance matching, a single electromagnetic wave attenuation mechanism and limited absorption bandwidth. In recent years, the emergence of new carbon-based EAMs such as carbon nanotubes (CNTs) and graphene nanosheets (GNs) has once again proved the application potential of carbon materials in the field of microwave absorption. Kong et al. [12] assembled cobalt tetrapyrrolineporphyrine (CoTAP) on the surface of multi-walled carbon nanotubes (MWCNTs) as a shell via a coordination bond. This kind of surface modification resulted in heterostructure on the heterogeneous interface, which enhanced the polarization loss and reduces the surface reflection. At a thickness of 2.1 mm, the minimum value of the reflection coefficient and the corresponding frequency of the optimal sample are -54.7 dB and 9.8 GHz, respectively. Compared with CNTs, graphene materials are often used as the supporting matrix of other EAMs to achieve an enhanced composite effect due to the special microplate structure. Qu et al. [13] developed a strategy for coupling hollow $\text{Fe}_3\text{O}_4/\text{Fe}$ nanoparticles with graphene sheets for high-performance

electromagnetic wave-absorbing material. The uniform loading of magnetic nanoparticles improved the impedance matching of single GNS and increased the magnetic loss mechanism. At a lower filling ratio of 18 wt%, the minimal reflection loss values of the composite could reach -30 dB at the absorber thickness ranging from 2.0 to 5.0 mm. However, the expensive preparation cost and the characteristics of easy agglomeration in the matrix limit the application of CNTs and GNs. In view of the above situation, carbon nanospheres are carbon-based materials with good potential. The low cost of preparation, simple and diverse preparation schemes have attracted widespread attention to the research of carbon nanospheres, and the roller effect brought by the spherical structure also provides favorable conditions for the uniform dispersion of carbon nanospheres in the matrix. Wu et al. [14] provided a facile method to development of bandwidth electromagnetic absorber via loading magnetic quantum dots on the mono-dispersed amorphous carbon sphere. At a filling ratio of 30 wt%, the sample calcined at 700 °C can obtain 5.8 GHz broadband absorption at ultra-thin thickness of 1.5 mm. Although the addition of magnetic components enhances the microwave absorbing properties of carbon nanospheres, it also leads to an increase in the filling rate (magnetic materials can only show better magnetism at a higher filling rate) and an increase in the weight of EAM. Therefore, it is still a challenge to develop a lightweight, broadband carbon nanospheres EAM.

In this work, we introduced a new method for preparing porous, hollow porous carbon spheres (HPC). Using two solgel processes reacting in the same alkaline environment, a core-shell precursor of silica coated with silica/phenolic resin spheres ($\text{SiO}_2@\text{SiO}_2/\text{PR}$) was prepared. By controlling the calcination temperature, the PR was converted into carbon with different graphitization degrees, and then the SiO_2 soft template was etched away with HF acid, and HPC with different dielectric properties was obtained. The special porous and hollow structure greatly reduces the material density, thereby reducing the filling rate, and provides a new channel for electromagnetic wave transmission, which brings excellent wave absorption performance to HPC. The simple preparation process and the advantages of ultralight materials provide a good application prospect for the carbon nanospheres prepared by this work.

Experiments

Reagents and raw materials

The specifications of the chemical reagents and raw materials used in this work are shown in Table 1.

Preparation of SiO₂@SiO₂/PR precursor

Ten milliliters of ethyl orthosilicate (TEOS) was added to a solution containing 200 mL ethanol, 30 mL water, and 12 mL ammonia and stirred for 15 min. Then, 1.76 g resorcinol and 2.46 mL formaldehyde were added to the solution and stirred mechanically for 18 h at room temperature. After centrifugation, washing with deionized water and ethanol for three times and drying at 50 °C overnight, the SiO₂@SiO₂/PR precursor was obtained.

Preparation of HPC with different dielectric properties

Using a vacuum high-temperature tube furnace, the precursor was heated to different temperatures at a heating rate of 2 °C/min in an Ar atmosphere, and the temperature was kept for 5 h. The calcined product was soaked in a 15% HF acid solution for 3 h to remove silica to obtain carbonized HPC. The samples with calcination temperatures of 500 °C, 600 °C, 700 °C and 800 °C were marked as HPC-1, HPC-2, HPC-3 and HPC-4, respectively.

Characterization

A scanning electron microscope (SEM, Hitachi, S-4800) and a transmission electron microscope (TEM, JEOL JEM-2100F) were used to observe the microscopic morphology and crystal surface growth of samples. A nitrogen adsorption and desorption

analyzer (Micromeritics Gemini VII 2390) was used to obtain the nitrogen adsorption and desorption curve of samples, and the BET and BJH models were used to calculate the specific surface area and pore size distribution, respectively. A Raman analyzer (Raman spectra, HORIBA, LabRAM HR Evolution) was used to obtain graphitization information of samples. In addition, a Fourier transform infrared spectroscopy (FT-IR, Nicolet, Nexus 670) and a high resistivity meter (HRM, Jingge Electronic, ST2643) were used to test the organic composition and resistivity of samples, respectively. The electromagnetic parameters of samples were obtained by vector network analyzer (VNA, Ceyear, 3672b), and the microwave absorbing properties were deduced. When testing the electromagnetic properties, the sample and paraffin were pressed into a ring with an outer diameter of 7 mm, an inner diameter of 3 mm and a thickness of about 2 mm according to the mass ratio of 0.5:9.5. According to the measured electromagnetic parameters (real and imaginary parts of complex permittivity: ϵ' and ϵ''), Eqs. (1) and (2) are used to calculate the reflection loss (R_L) of samples [15]:

$$Z_{in} = Z_0(\mu_r/\epsilon_r)^{1/2} \tanh \left[j(2\pi f d (\mu_r \epsilon_r)^{1/2})/c \right] \quad (1)$$

$$R_L(\text{dB}) = 20 \log |(Z_{in} - Z_0)/(Z_{in} + Z_0)| \quad (2)$$

where Z_{in} is the input impedance of the absorber, f is the frequency of the electromagnetic wave, d is the coating thickness of the absorber and c represents the velocity of electromagnetic wave in free space, ϵ_r ($\epsilon_r = \epsilon' - j\epsilon''$) and μ_r ($\mu_r = \mu' - j\mu''$) are the complex permittivity and permeability, respectively. It is generally considered that the frequency band $R_L < -10$ dB is the effective absorption band (f_E), which represents the attenuation efficiency of electromagnetic wave $> 90\%$ [16].

Results and discussion

Preparation mechanism and microstructure

Figure 1 shows the typical preparation process of HPC. The preparation of the SiO₂@SiO₂/PR precursor involves two solgel processes under alkaline conditions: 1. Under alkaline conditions, OH⁻ attacks the Si atoms in TEOS, causing nucleophilic substitution and breaking the Si–O bond, completing the hydrolysis reaction; subsequently, the condensation

Table 1 Material specifications used in this work

Reactant	Manufacture	Purity %
Tetraethyl silicate	Aladdin, China	> 99.0
Anhydrous ethanol	Nanjing Reagent, China	> 99.5
Ammonia (25–28%)	Aladdin, China	> 99.9
Resorcinol	Aladdin, China	97.0
Formaldehyde (35–40%)	Nanjing Reagent, China	+ 98.0
Hydrofluoric acid (40%)	Macklin, China	> 95.0

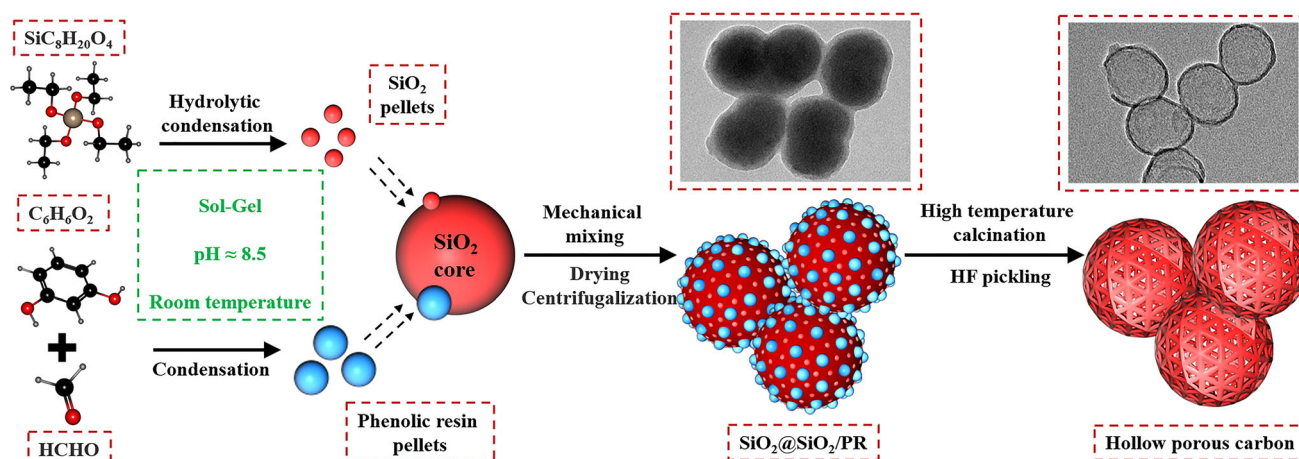


Figure 1 The typical preparation process of HPC, including two kinds of sol-gel process, calcination and pickling treatment.

reaction occurs between the $-\text{Si}-\text{OH}$ generated by the hydrolysis, and the $-\text{Si}-\text{O}-\text{Si}-$ is formed, and the water molecules are removed at the same time. As the hydrolysis and condensation reactions proceed, tiny, dispersed sol particles appear in the system. These colloidal particles form a spatially open skeleton structure (gel) through Van der Waals forces, hydrogen bonds or chemical bonds and are transformed into SiO_2 particles. 2. Under alkaline conditions, resorcinol and formaldehyde will undergo a sol-gel reaction at a molar ratio of about 1:2, divalent phenolic alcohols with different molecular structures are first generated, and then intermolecular condensation forms linear resol phenolic resin, which is gradually transformed into PR. Due to the Van der Waals force, the PR beads will be adsorbed on the surface of the larger SiO_2 particles in the system, and the small SiO_2 particles generated by the subsequent hydrolysis and condensation of TEOS will also be adsorbed by the larger SiO_2 particles, and finally the $\text{SiO}_2@/\text{SiO}_2/\text{PR}$ precursor is obtained. The prepared precursor is calcined in an inert atmosphere at a high temperature. During this process, the thermally stable SiO_2 will not be affected, while the organic PR will be transformed into partially crystalline carbon to form $\text{SiO}_2@/\text{SiO}_2/\text{C}$ intermediate product. After HF pickling, SiO_2 on the surface and inside is etched away to obtain HPC. The degree of graphitization of HPC can be adjusted by the calcination temperature.

A scanning electron microscope was used to observe the microscopic morphology of the product at each stage, as shown in Fig. 2. The prepared $\text{SiO}_2@/\text{SiO}_2/\text{PR}$ precursors are nano-sized spheres of uniform size, with a diameter of about 90–120 nm.

The spheres are closely connected under the action of static electricity and agglomerate on a small scale, as shown in Fig. 2a and b. Under the protection of inert gas, high temperature will convert organic PR into carbon, while SiO_2 with good thermal stability will not be affected. Due to the decomposition of small molecular substances in a high-temperature environment, the spherical shell is partially recessed, and the pattern-like structure on the surface of the nanospheres in Fig. 2d is the small SiO_2 particles without recesses. After HF pickling treatment, the small SiO_2 particles and SiO_2 core on the surface of spheres react with HF acid and escape in the form of SiF_4 gas, leaving a porous, hollow structure composed of carbon, which is HPC. HPC maintains the apparent morphology of the precursor, a small part of HPC is broken due to high-temperature internal stress, and the hollow structure can be clearly seen from the broken spheres. As the calcination temperature increases, the number of crushing HPC increases, as shown in Fig. 2e–h.

Figure 3 shows the pictures of the products at each stage under the transmission electron microscope. The $\text{SiO}_2@/\text{SiO}_2/\text{PR}$ precursor exhibits a typical core-shell structure. The large SiO_2 particles inside cannot pass through the electron beam due to the solid structure, and the color is darker, while the shell composed of small SiO_2 particles and small PR particles has a lighter color due to the gaps between the particles, as shown in Fig. 3a and b. The prepared HPC shows a clear hollow structure, the diameter of the nanospheres is about 110 nm, and the thickness of the shell is about 7 nm. Such a thin shell thickness and hollow structure help greatly reduce the material

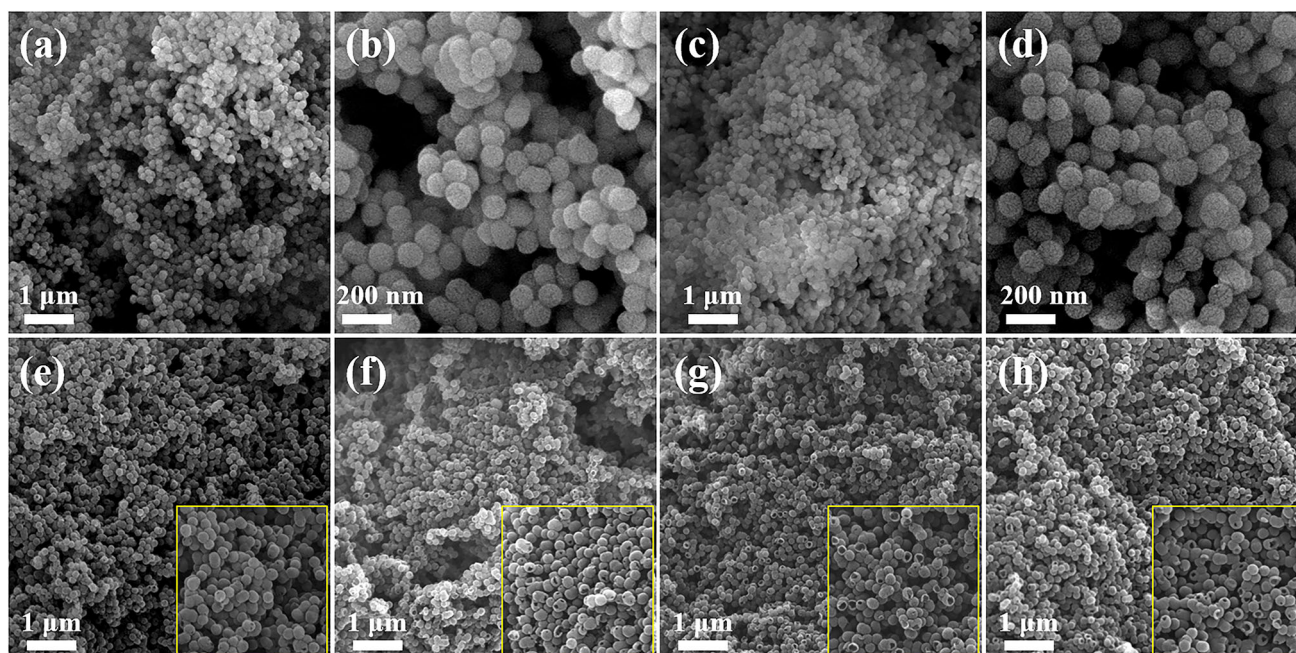
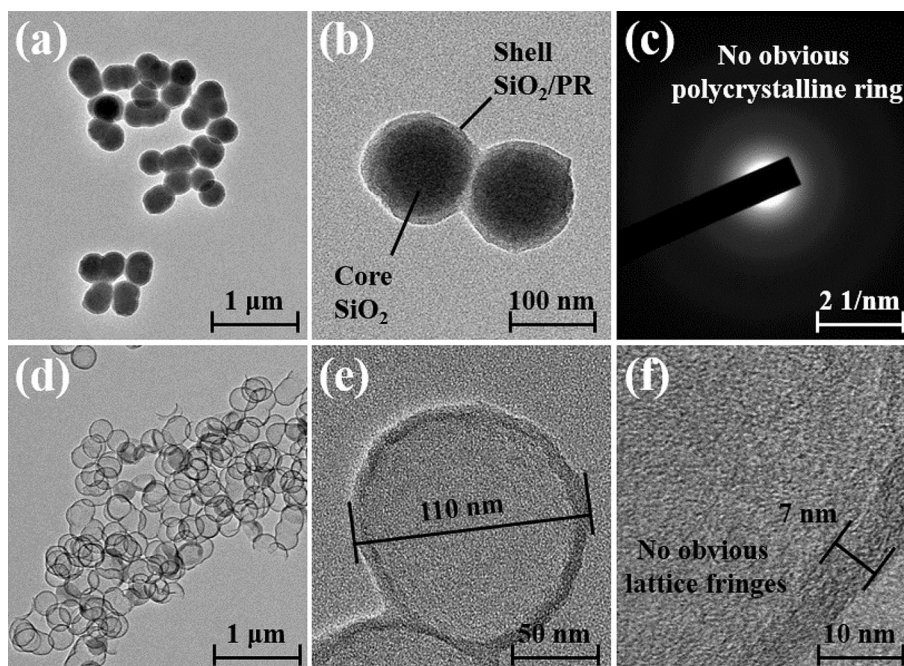


Figure 2 SEM images of **a, b** $\text{SiO}_2@\text{SiO}_2/\text{PR}$ precursor; **c, d** $\text{SiO}_2@\text{SiO}_2/\text{C}$ intermediate products, not pickled; **e–h** HPC-1, HPC-2, HPC-3, HPC-4, respectively.

Figure 3 HRTEM images of products in each stage. **a, b** $\text{SiO}_2@\text{SiO}_2/\text{PR}$ precursor; **c** selected area electron diffraction pattern of HPC-3; **d–f** HRTEM images of HPC-3 in the scale of 1 μm , 50 nm and 10 nm, respectively.



density, as shown in Fig. 3d–f. Because the surface pore size is very small, it cannot be clearly found in the TEM image, and it needs to be further characterized by nitrogen adsorption–desorption (see later). The obvious multi-wafer rings and lattice stripes cannot be found in Fig. 3c and f, which proves that

the HPC prepared by this work has a low degree of graphitization.

Basic properties

Figure 4a shows the FT-IR spectra of the four sets of samples and precursors. Among them, the absorption

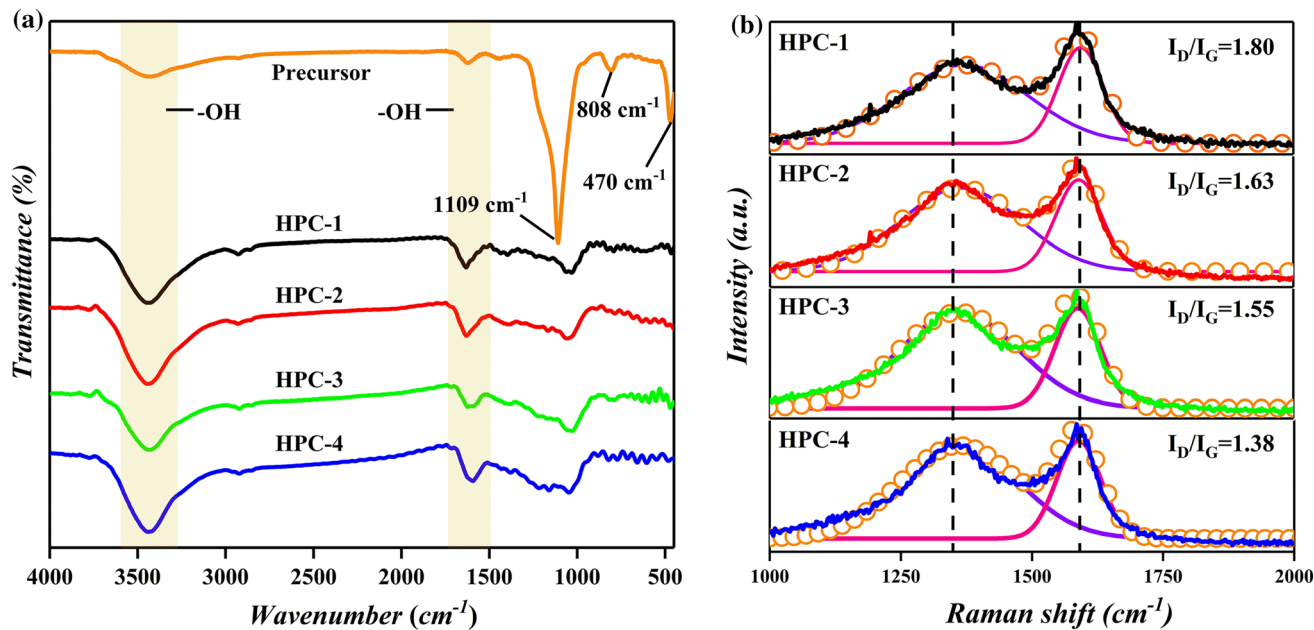


Figure 4 a Fourier infrared spectra (4000–450 cm^{-1}) and b Raman spectra (1000–2000 cm^{-1}) of products in each stage.

peaks at 3400 cm^{-1} and 1640 cm^{-1} come from the stretching vibration and bending vibration of -OH , which are mainly caused by the unremoved water in the sample. For the precursor, there are obvious absorption peaks at 470 cm^{-1} , 808 cm^{-1} and 1109 cm^{-1} , which are the characteristic absorption regions of Si-O . It is worth mentioning that, compared with the standard FT-IR spectrum, the characteristic absorption region of Si-O has a redshift (moving to a high wave number). This is because the carbon element with high electronegativity creates attraction to the outermost electrons of silica, which causes the electron density to change. When calcined at high temperature and etched with hydrofluoric acid, the absorption peaks of silica of all samples disappeared, showing a typical FT-IR spectrum of inorganic substances. From the Raman spectra in Fig. 4b, the degree of graphitization of carbon at different calcination temperatures can be analyzed. It is known to all that the peak near 1360 cm^{-1} corresponds to the vibration of sp^3 carbon atoms in disordered graphite (called D band), and the peak near 1580 cm^{-1} corresponds to the in-plane vibration of sp^2 carbon atoms in the two-dimensional hexagonal lattice (called G band) [17]. The ratio of D band to G band ($I_{\text{D}}/I_{\text{G}}$) is often used to evaluate the degree of graphitization of carbon materials [18, 19]. According to the peak area fitting results, it is found that the $I_{\text{D}}/I_{\text{G}}$ of the samples calcined at $500\text{--}800\text{ }^{\circ}\text{C}$ is 1.80, 1.63, 1.55 and 1.38,

respectively. With the increase in the calcination temperature, the $I_{\text{D}}/I_{\text{G}}$ of the sample decreases, indicating an increase in the degree of graphitization. Since the dielectric properties of highly crystalline carbon are much better than those of amorphous carbon, this increase in crystallinity indicates that HPC prepared at high calcination temperatures may have better dielectric properties.

For porous materials, nitrogen adsorption and desorption tests can be carried out to obtain information about pore properties, pore size distribution and BET specific surface area. Figure 5 shows the isothermal nitrogen adsorption and desorption curves of the four groups of samples. Each group of samples exhibits a long and narrow hysteresis loop, showing a certain nitrogen adsorption capacity, which is a characteristic of porous materials. However, due to the small number of pores, the area of the hysteresis ring is also small, which is not a characteristic of typical microporous or mesoporous materials. The BJH pore size distribution model also proves this point. The sample has a small number of pores, and the pore size is mainly distributed in the range of micropores and mesopores. The average pore width calculated by BJH model is 6.44 nm, 8.16 nm, 8.61 nm and 9.19 nm, respectively. In addition, the maximum pore volume of HPC-1, HPC-2, HPC-3 and HPC-4 is, respectively, $0.55\text{ cm}^3/\text{g}$, $0.83\text{ cm}^3/\text{g}$, $1.26\text{ cm}^3/\text{g}$ and $1.12\text{ cm}^3/\text{g}$, indicating

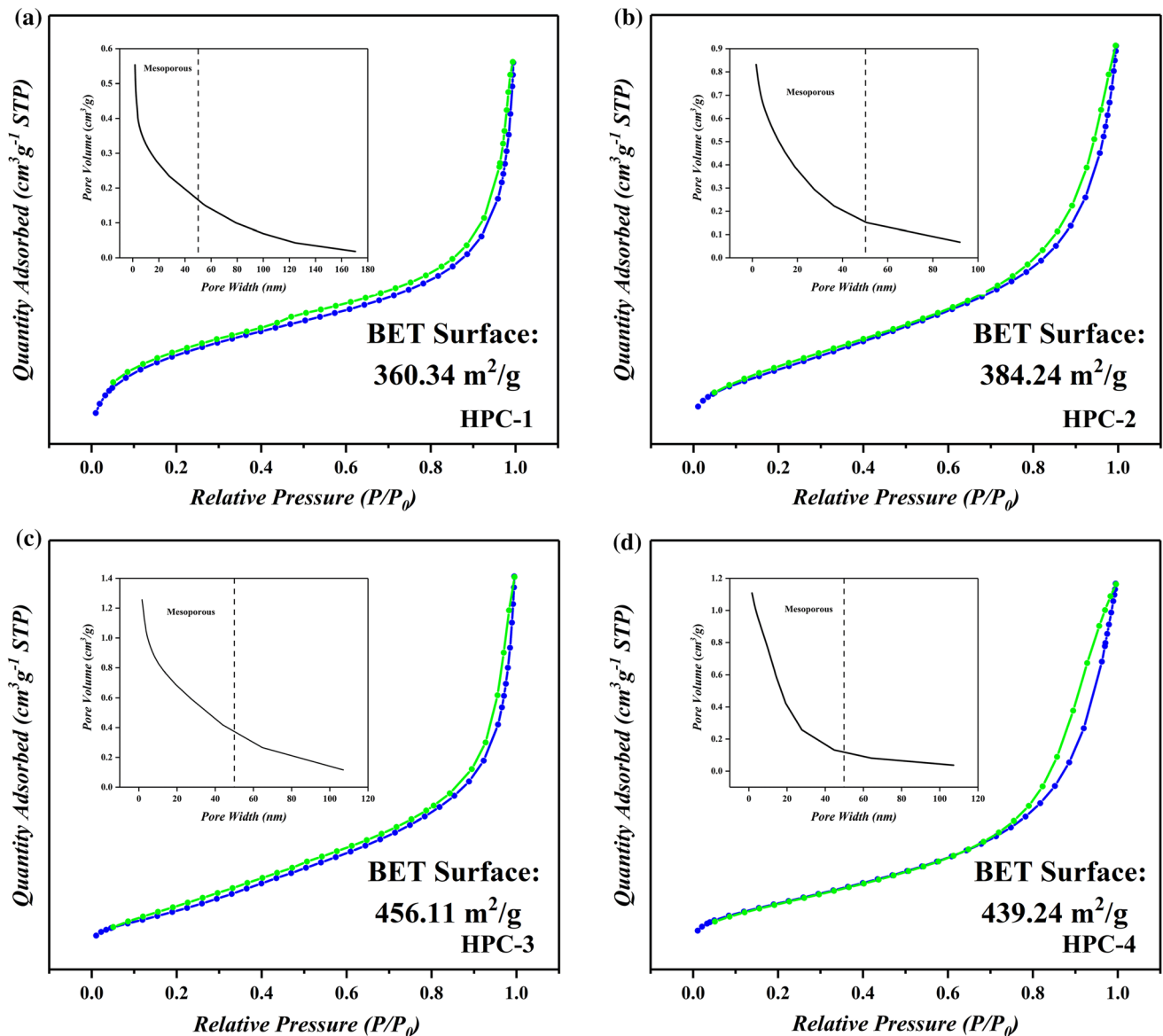


Figure 5 Nitrogen adsorption-desorption curve and BJH pore size distribution model of samples; the BET specific surface area of each sample is also shown in figures.

that the increase in calcination temperature will increase the number of pores first and then decrease. This is because the heat treatment at higher temperature will produce stronger internal stress, and the complete spherical structure of hollow carbon spheres is more likely to collapse, break and form more holes under the effect of internal stress. The change trend of the BET specific surface area is the same. The BET specific surface areas of the four groups of samples are $360.34 \text{ m}^2/\text{g}$, $384.24 \text{ m}^2/\text{g}$, $456.11 \text{ m}^2/\text{g}$ and $439.24 \text{ m}^2/\text{g}$, respectively. Such a large specific surface area can provide more

scattering and reflection points for electromagnetic wave conduction [20] and significantly improve the electromagnetic wave attenuation efficiency.

Dielectric properties

Since carbon materials are typical non-magnetic materials, only the influence of the dielectric properties of HPC on its microwave absorbing properties will be discussed here. The complex permittivity of each sample was measured using the coaxial method, as shown in Fig. 6a and b. It is well known that the real part represents its storage capacity for

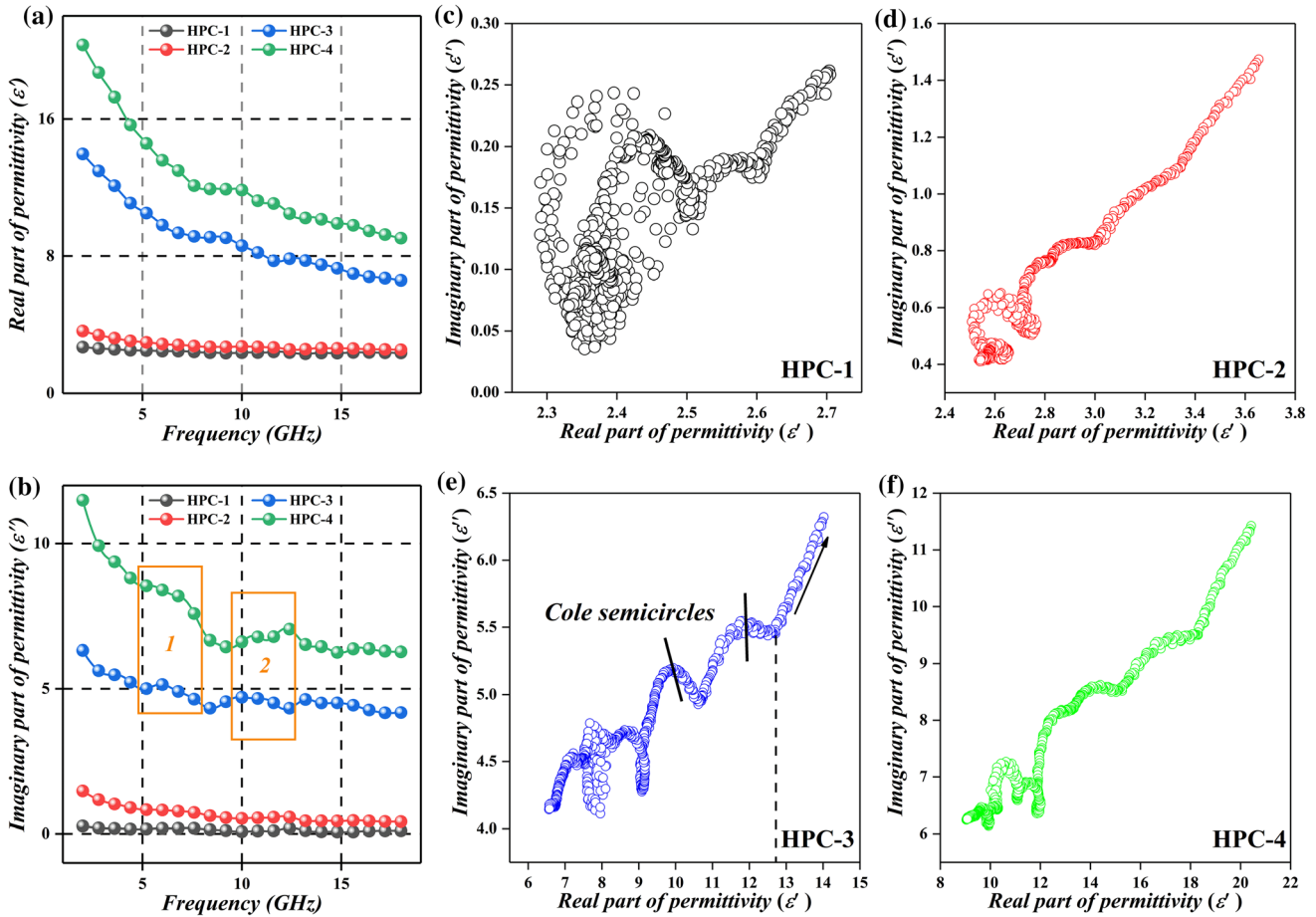


Figure 6 **a** Real part of permittivity (ϵ') and **b** imaginary part of permittivity (ϵ'') of samples; the box in **b** shows the region of dipole polarization; **c–f** typical Cole–Cole semicircles of HPC-1,

HPC-2, HPC-3 and HPC-4, respectively, showing the intensity of the dipole polarization of each sample.

electromagnetic energy, and the virtual part represents its attenuation capacity for electromagnetic energy [21, 22]. For HPC, as the calcination temperature increases, both ϵ' and ϵ'' increase significantly. This is because a high calcination temperature is conducive to the improvement in carbon crystallinity, which improves the energy storage capacity and loss capacity of HPC. It is worth mentioning that the ϵ' and ϵ'' curves of HPC-3 and HPC-4 have some significant peaks. According to the free electron theory, if the dielectric loss of the absorbing material mainly comes from the conductance loss, the ϵ' and ϵ'' curves will be a decreasing curve with increasing frequency [23]; if there is polarization phenomenon, the curve will show multiple undulating peaks [24]. The appearance of these peaks signifies the existence of polarization, and the aggravation of this electric dispersion phenomenon is conducive to the expansion of the effective bandwidth. In addition, two

significant relaxation peaks can be observed in the ϵ'' curve. In the microwave band, the contribution of electron polarization and ion polarization to the polarization phenomenon is very small and generally ignored; thus, these relaxation peaks often come from the relaxation phenomenon caused by the polarization of the dipole.

For dipole polarization, the Cole–Cole model can be used to characterize the degree of dipole polarization. ϵ' and ϵ'' can be derived using the Debye relaxation equations [25, 26]:

$$\epsilon' = \epsilon_\infty + \frac{\epsilon_s - \epsilon_\infty}{1 + (2\pi f)^2 \tau^2} \tag{3}$$

$$\epsilon'' = \frac{2\pi f \tau (\epsilon_s - \epsilon_\infty)}{1 + (2\pi f)^2 \tau^2} \tag{4}$$

$$(\epsilon' - \epsilon_\infty)^2 + (\epsilon'')^2 = (\epsilon_s - \epsilon_\infty)^2 \tag{5}$$

where ϵ_s is the static dielectric constant, ϵ_∞ is the optical permittivity at high frequency limit and τ is the relaxation period. According to Eq. (5), a Cole–Cole circle model with ϵ' as the X-axis and ϵ'' as the Y-axis can be drawn, as shown in Fig. 6c–f. Each Cole semicircle represents a Debye dipole polarization phenomenon. The number and radius of the Cole semicircle reflect the degree of polarization of the dipole. HPC-1 does not show obvious Cole circles. With the increase in the calcination temperature, the number and radius of Cole circles increase significantly, reflecting the significant increase in dipole polarization. Taking HPC-3 as an example, when ϵ' is large (low frequency), the Cole curve is a straight line, and the dielectric loss of this section is dominated by conduction loss; when ϵ' is small (middle and high frequency), two significant semicircles appear in the Cole curve, and the dielectric loss in this section is dominated by polarization loss. The position of the semicircle is consistent with the position marked by the box in Fig. 6b, which confirms that the two resonance peaks come from the dipole polarization.

Using the dielectric loss factor ($\tan\delta_e$, $\tan\delta_e = \epsilon''/\epsilon'$) can more intuitively analyze the changes of dielectric loss capability of samples, as shown in Fig. 7a. The $\tan\delta_e$ of HPC increased greatly with the increase in calcination temperature. Among them, the $\tan\delta_e$ of HPC-1 and HPC-2 decreased with increasing frequency, while the $\tan\delta_e$ of HPC-3 and HPC-4 increased with increasing frequency. Since dielectric loss is often divided into conductance loss and polarization loss, it is necessary to discuss the proportion of conductance loss and polarization loss in dielectric loss for pure dielectric carbon materials. According to Debye theory [20]:

$$\epsilon''(\omega) = \epsilon''_p + \epsilon''_c = (\epsilon_s - \epsilon_\infty) \frac{\omega\tau}{1 + \omega^2\tau^2} + \frac{\sigma}{\epsilon_0\omega} \quad (6)$$

where ϵ''_p and ϵ''_c represent polarization loss part and conductance loss part, respectively, ω is the angular frequency, σ is the electrical conductivity and τ is the relaxation time. According to Eq. (6), a nonlinear equation is used to fit the test results, and the fitted conductance loss and polarization loss are shown in Fig. 7b and c. The conductance loss shows a decreasing trend with the increase in frequency, and the polarization loss shows an increasing trend with the increase in frequency. With the increase in the calcination temperature, the conductivity loss and

polarization loss of HPC are significantly enhanced. The change of $\tan\delta_e$ with the frequency change trend comes from the compensation effect of polarization loss on conductance loss in the middle- and high-frequency regions.

Moreover, the complex permittivity of a material at high frequencies has a corresponding relationship with its static resistivity. According to the free electron theory [27]:

$$\rho = 1/\pi f \epsilon'' \epsilon_0 \quad (7)$$

where ρ is the resistivity and f is the electromagnetic field frequency corresponding to a value of ϵ'' . The decrease in resistivity is conducive to the enhancement of the material's dielectric loss capability. Figure 7d shows the measured resistivity of each sample. As the calcination temperature rises, the resistivity of the sample decreases significantly. This is because a higher calcination temperature is beneficial to increase the degree of graphitization of carbon materials and promote carriers migration. The decrease in resistivity corresponds to the increase in dielectric loss, which confirms the view of free electron theory.

A good EAM needs to take into account impedance matching and electromagnetic wave attenuation, that is, to allow electromagnetic waves to enter the material to the greatest extent and efficiently attenuate electromagnetic wave energy. Through Eqs. (8–11), the impedance matching and attenuation characteristics of samples can be characterized [22, 25]:

$$R = \frac{Z_0 - Z_{in}}{Z_0 + Z_{in}} \quad (8)$$

$$Z_{in} = \sqrt{\frac{\mu_r \mu_0}{\epsilon_r \epsilon_0}} \quad (9)$$

$$Z_0 = \sqrt{\frac{\mu_0}{\epsilon_0}} \quad (10)$$

$$\alpha = \frac{\sqrt{2}\pi f}{c} \times \sqrt{(\mu''\epsilon'' - \mu'\epsilon') + \sqrt{(\mu''\epsilon'' - \mu'\epsilon')^2 + (\mu'\epsilon'' + \mu''\epsilon')^2}} \quad (11)$$

where R represents the reflection coefficient, Z_0 represents the impedance of air, Z_{in} represents the wave impedance at interface, μ_0 is the vacuum permeability, ϵ_0 is the vacuum permittivity and c represents the speed of light in a vacuum. Figure 7 e and f, respectively, shows the samples' α and impedance

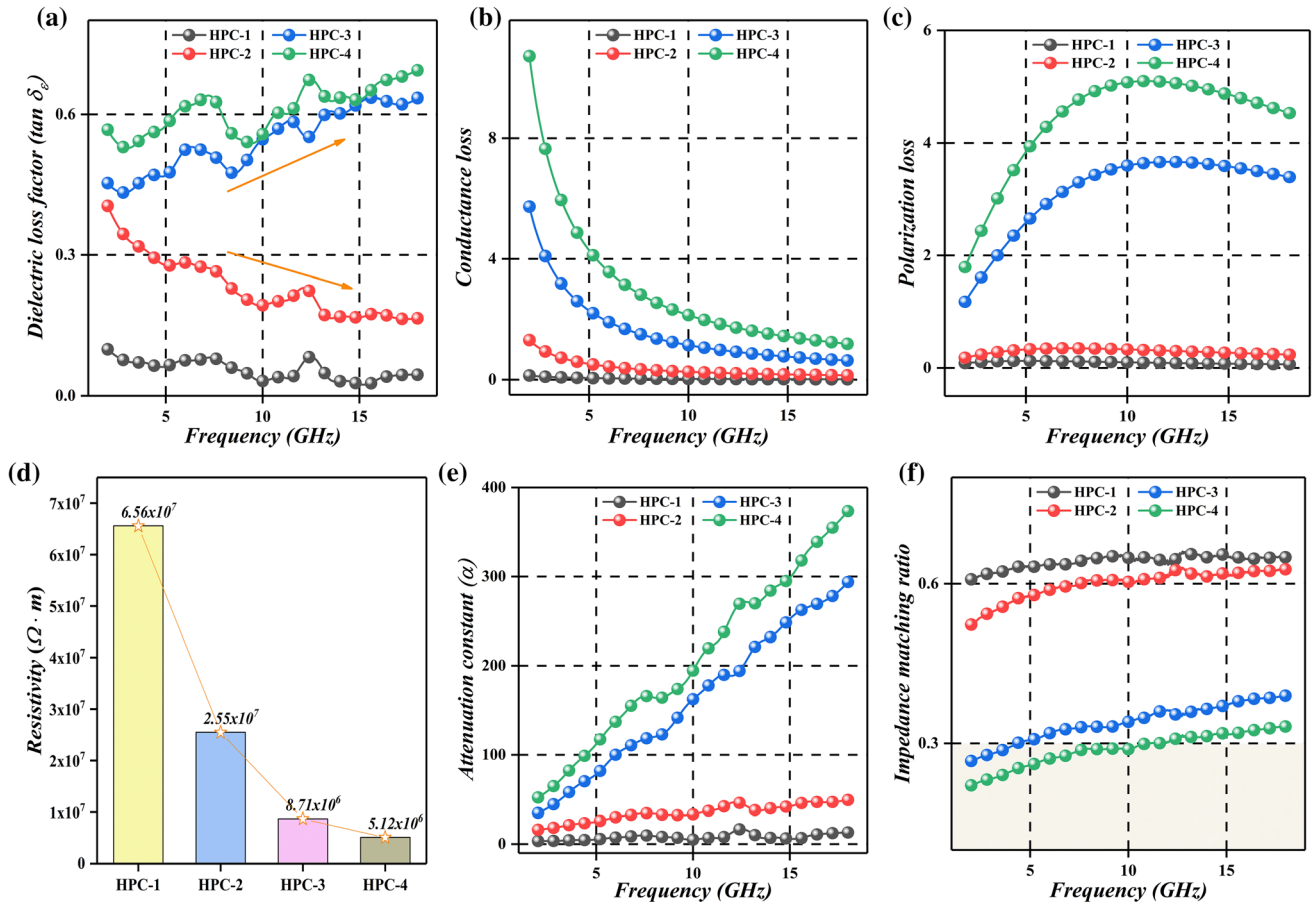


Figure 7 a Dielectric loss factor ($\tan \delta_e$) of samples; b, c conductance loss part and polarization loss part of dielectric loss fitted by Debye theory of samples; d measured resistivity of samples; e, f attenuation constant α and impedance matching ratio of samples.

matching ratio with frequency. As the frequency increases, α and impedance matching ratio gradually increase, which indicates that the prepared HPC may obtain good absorbing performance in the middle- and high-frequency regions. It is generally believed that materials with an impedance matching ratio higher than 0.3 can effectively allow electromagnetic waves to enter and attenuate electromagnetic wave energy [25]. Although HPC-4 has a higher α than HPC-3, its absorbing performance may be limited due to poor impedance matching (the impedance matching ratio in 2–10 GHz < 0.3).

Wave absorbing performance

According to Eqs. (1) and (2), the R_L of samples is derived, and the three-dimensional representation model of R_L of each sample is drawn as shown in Fig. 8. HPC-1 has almost no absorbing properties, while HPC-2 has certain absorbing properties only

under a large thickness. In comparison, HPC-3 and HPC-4 have very excellent absorption performance: HPC-3 has an R_{Lmin} of -23.35 dB at 3 mm and an f_E of 5.73 GHz at 2 mm; HPC-4 has an R_{Lmin} of -14.36 dB at 2.2 mm and an f_E of 4.11 GHz at 1.5 mm. Interestingly, in the three-dimensional model, HPC-3 and HPC-4 have multiple dual regions with excellent absorbing properties—reversed islands. Most of these reversed islands are concentrated in the quarter-wavelength region. As a typical interference absorbing material, when the matching thickness reaches a critical value ($> 3/4 \lambda$), there will often be more than two absorption peaks due to the interference and cancellation phenomenon of the incident electromagnetic wave and the reflected electromagnetic wave [28]. On the whole, HPC-3 has the best absorbing performance, thanks to its moderate impedance matching characteristics and electromagnetic wave attenuation ability.

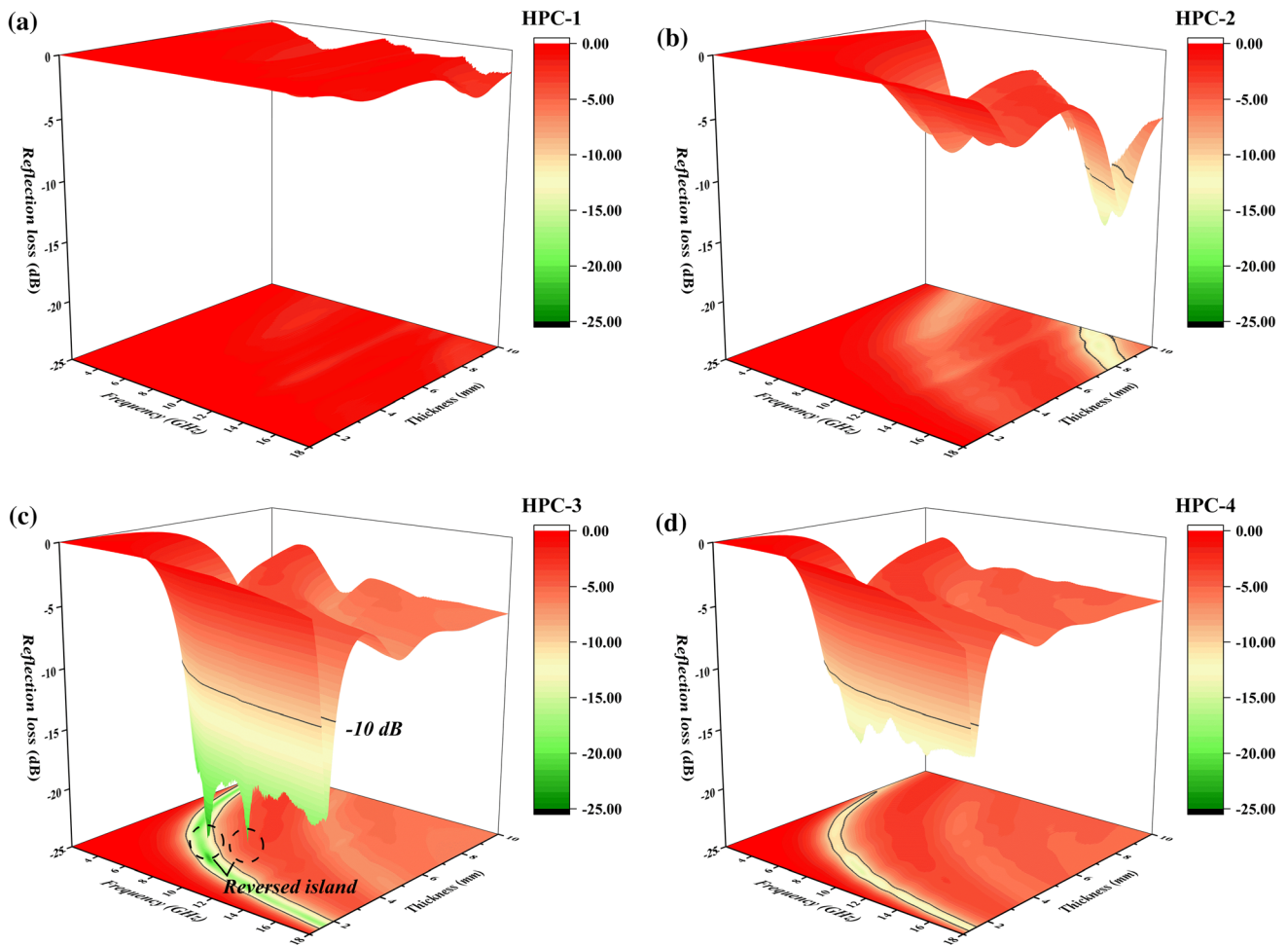


Figure 8 a–d Three-dimensional representation of the values of reflection loss for HPC-1, HPC-2, HPC-3 and HPC-4, respectively.

Figure 9 shows the R_L under different thicknesses, two-dimensional representation models of R_L , f_E under different thicknesses and quarter-wavelength regions of HPC-3 and HPC-4. From Fig. 9a, c, e, g, it can be seen that as the material thickness increases, the corresponding absorption frequency band moves to the low-frequency direction. This movement can be explained by the quarter-wavelength equation [29]:

$$t_m = nc/4f_m(\mu_r\epsilon_r)^{1/2}(n = 1, 3, 5, \dots) \quad (12)$$

where t_m is the matching thickness and f_m represents the frequency corresponding to the complex permeability and complex permittivity. In addition, it can be seen from Eq. (12) that larger electromagnetic parameters are beneficial to reduce the matching thickness. The increase in the calcination temperature increases the permittivity, which is beneficial to the preparation of thin-layer wave-absorbing materials.

By controlling the thickness of the absorbing layer, HPC can obtain absorbing performance in multiple frequency bands, and the application range is very flexible. Combining Fig. 9a, b, e, f, it can be seen that the measured $R_{L\min}$ is basically consistent with the position of the quarter wavelength ($1/4\lambda$) derived from the electromagnetic parameters, which proves that the excellent matching characteristics at $1/4\lambda$ contribute to the improvement in the absorption strength. Figure 9d and h shows the f_E of HPC under different thicknesses. Under the thinner thickness less than 3 mm, HPC has excellent absorbing properties.

Figure 10 shows the possible electromagnetic attenuation mechanism of the HPC prepared in this work in the paraffin matrix. When the incident electromagnetic wave enters the coaxial ring sample and contacts with HPC, the special hollow structure makes the inner and outer layers of the HPC shell be

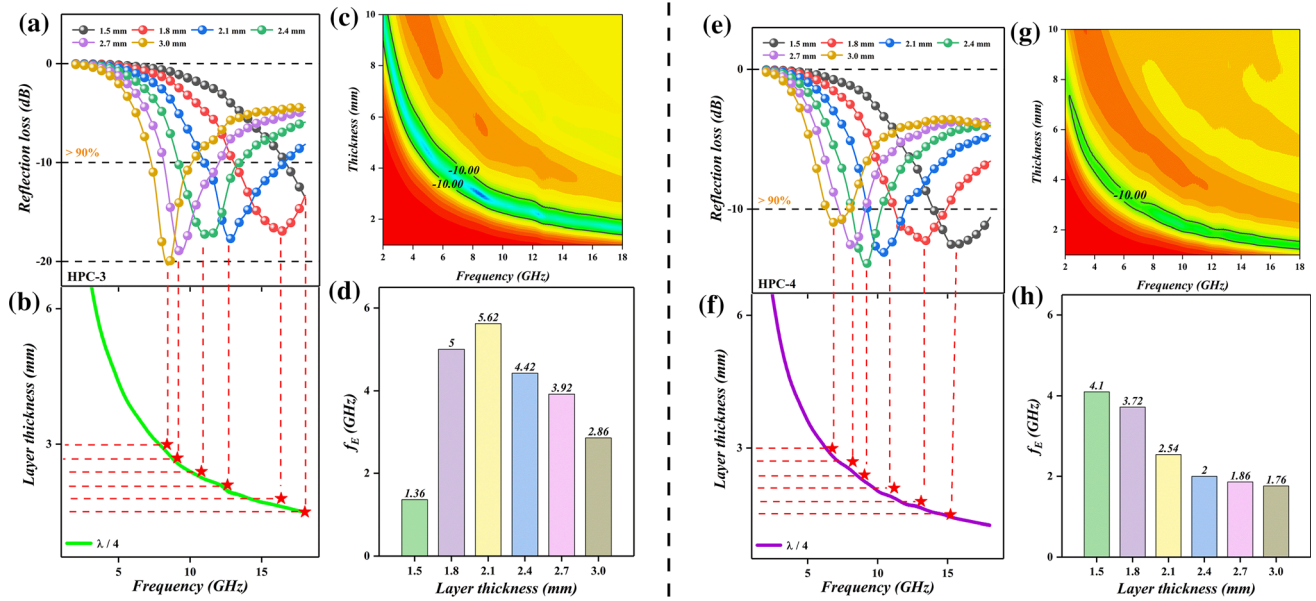


Figure 9 a R_L corresponding to different thicknesses, b quarter-wavelength region, c two-dimensional representation of the values of reflection loss and d f_E under different thicknesses of HPC-3;

e R_L corresponding to different thicknesses, f quarter-wavelength region, g two-dimensional representation of the values of reflection loss and h f_E under different thicknesses of HPC-4.

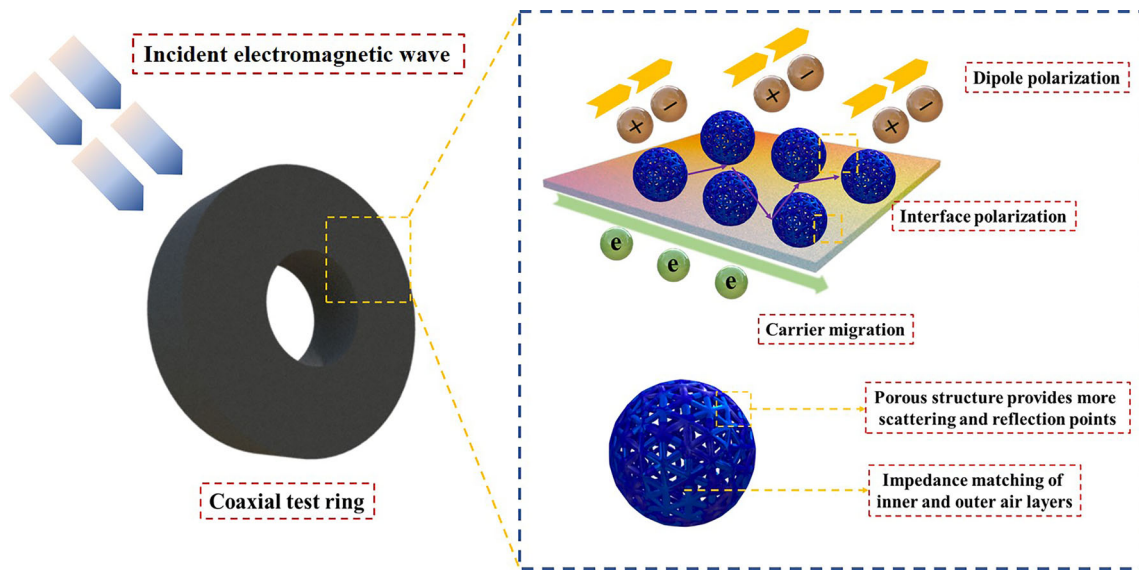


Figure 10 Possible attenuation mechanism of electromagnetic wave in HPC.

the same air layers, and the impedance matching is greatly improved, which allows more electromagnetic waves to enter the material and cause loss instead of reflecting off on the surface of the material. The special porous structure and higher specific surface area provide more scattering and reflection points for electromagnetic wave conduction, which greatly improves the attenuation efficiency of electromagnetic waves. The appropriate degree of

graphitization enables HPC to have good dielectric loss capability. Among them, free carbon and lattice defects can be used as the center of dipole polarization to promote the occurrence of dipole polarization; and the large π bond electrons in carbon atoms can migrate between carbon particles to form micro-current, which will consume electromagnetic wave energy in the form of thermal energy. Moreover, the heterogeneous interface between HPC and the

Table 2 Performance comparison of HPC with other carbon-absorbing agents reported in recent years

Absorber	Absorber content (wt%)	Matching thickness (mm)	R_{Lmin} (dB)	f_E (GHz)	References
rGO/ZnO	15	2.4	– 54.2	6.7	[24]
CNTs/Fe ₃ O ₄ /ZnO	30	2.5	– 40.9	2.4	[32]
Fe ₃ O ₄ /C	40	2.4	– 45.3	2.3	[33]
Porous Fe ₃ O ₄ /C	71.5	3.0	– 31.75	5.12	[34]
C@Fe ₃ O ₄ @Fe	50	1.5	– 40	5.2	[18]
C/Fe/Fe ₃ O ₄ QDs	30	1.5	– 26.2	5.8	[14]
rGO/Ni	20	2.7	– 59.7	4.8	[35]
HPC-3	5	2	– 23.35	5.73	This work
HPC-4	5	1.5	– 14.36	4.11	This work

paraffin matrix will accumulate a large amount of charge due to the Maxwell–Wagner effect, resulting in interface polarization [30, 31]. The synergy brought by the special hollow, porous structure and the reasonable degree of graphitization are the main reasons for HPC to obtain excellent wave absorbing performance.

Table 2 shows the comparison between HPC prepared in this work and some carbon-absorbing materials reported in recent years. With an ultra-low filling ratio of 5 wt%, HPC can achieve broadband absorption at a thinner thickness. In addition, most carbon-based absorbing agents are combined with other absorbing agents to obtain enhanced absorbing performance, which not only increases the cost of raw materials and the difficulty of preparation, but also reduces the lightweight advantage of carbon-based absorbing agents. Compared with this, by constructing a special porous and hollow structure to enhance the absorbing performance of the carbon-based wave-absorbing agent, it undoubtedly has a better application prospect.

Conclusions

In summary, this work provides a simple solution for preparing hollow and porous carbon nanospheres using SiO₂ as a soft template. The prepared HPC has a particle size of about 100 nm and a shell thickness of less than 10 nm, and its dielectric properties can be easily adjusted by controlling the calcination temperature. The special hollow and porous structure not only greatly reduces the density, but also improves the impedance matching, and provides a new channel for the transmission of electromagnetic

waves. The larger specific surface area also improves the attenuation efficiency of electromagnetic waves to a certain extent. With an ultra-low filling ratio of 0.5:9.5, HPC can obtain an effective bandwidth of 5.73 GHz at a thickness of 2 mm. It is a lightweight and efficient electromagnetic wave absorber. Considering the low preparation cost and simple preparation scheme, HPC is expected to become one of the candidates for high-efficiency electromagnetic wave absorbers. Moreover, the hollow and porous structure can promote the electromagnetic wave attenuation ability of materials, which also provides a new idea for improving the performance of absorbing agent.

Acknowledgements

This work is supported by the National Natural Science Foundation of China (51702158).

Compliance with ethical standards

Conflict of interest The authors declare that they have no conflict of interest.

References

- [1] Sun XX, Yang ML, Yang S, Wang SS, Yin WL, Che RC, Li YB (2019) Ultrabroad band microwave absorption of carbonized waxberry with hierarchical structure. *Small* 15:1902974
- [2] Lv HL, Yang ZH, Ong SJH, Wei C, Liao HB, Xi SB, Du YH, Ji GB, Xu ZCJ (2019) A flexible microwave shield with tunable frequency-transmission and electromagnetic compatibility. *Adv Funct Mater* 29:1900163

- [3] Li JS, Huang H, Zhou YJ, Zhang CY, Li ZT (2017) Research progress of graphene-based microwave absorbing materials in the last decade. *J Mater Res* 32:1213–1230
- [4] Zhao B, Deng JS, Zhao CX, Wang CD, Chen YG, Hamidinejad M, Li RS, Park CB (2020) Achieving wide-band microwave absorption properties in PVDF nanocomposite foams with an ultra-low MWCNT content by introducing a microcellular structure. *J Mater Chem C* 8:58–70
- [5] Feng AL, Hou TQ, Jia ZR, Wu GL (2020) Synthesis of a hierarchical carbon fiber@cobalt ferrite@manganese dioxide composite and its application as a microwave absorber. *RSC Adv* 10:10510–10518
- [6] Zhong M, Fei P, Fu XR, Lei ZQ, Su BT (2013) Synthesis of PS-CoFe₂O₄ composite nanomaterial with improved magnetic properties by a one-step solvothermal method. *Ind Eng Chem Res* 52:8230–8235
- [7] Zhu YF, Ni QQ, Fu YQ, Natsuki T (2013) Synthesis and microwave absorption properties of electromagnetic functionalized Fe₃O₄-polyaniline hollow sphere nanocomposites produced by electrostatic self-assembly. *J Nanopart Res* 15:1988
- [8] Wang G, Gao Z, Wan G, Lin S, Yang P, Qin Y (2014) High densities of magnetic nanoparticles supported on graphene fabricated by atomic layer deposition and their use as efficient synergistic microwave absorbers. *Nano Res* 7:704–716
- [9] Lv H, Guo Y, Zhao Y, Zhang H, Zhang B, Ji G (2016) Achieving tunable electromagnetic absorber via graphene/carbon sphere composites. *Carbon* 110:130–137
- [10] Meng FB, Wang HG, Huang F, Guo YF, Wang ZY, Hui D, Zhou ZW (2018) Graphene-based microwave absorbing composites: a review and prospective. *Compos Part B-Eng* 137:260–277
- [11] Ye W, Li W, Sun Q, Yu J, Gao Q (2018) Microwave absorption properties of lightweight and flexible carbon fiber/magnetic particle composites. *RSC Adv* 8:24780–24786
- [12] Kong L, Wang C, Yin XW, Fan XM, Wang W, Huang JF (2017) Electromagnetic wave absorption properties of a carbon nanotube modified by a tetrapyrroline porphyrine interface layer. *J Mater Chem C* 5:7479–7488
- [13] Qu B, Zhu C, Li C, Zhang X, Chen Y (2016) Coupling hollow Fe₃O₄-Fe nanoparticles with graphene sheets for high-performance electromagnetic wave absorbing material. *ACS Appl Mater Inter* 8:3730–3735
- [14] Wu GL, Cheng YH, Yang ZH, Jia ZR, Wu HJ, Yang LJ, Li HL, Guo PZ, Lv HL (2018) Design of carbon sphere/magnetic quantum dots with tunable phase compositions and boost dielectric loss behavior. *Chem Eng J* 333:519–528
- [15] Wen SL, Liu Y, Zhao XC, Cheng JW, Li H (2014) Synthesis, dual-nonlinear magnetic resonance and microwave absorption properties of nanosheet hierarchical cobalt particles. *Phys Chem Chem Phys* 16:18333–18340
- [16] Wang L, Quan Q, Zhang L, Cheng L, Lin P, Pan S (2018) Microwave absorption of NdFe magnetic powders tuned with impedance matching. *J Magn Magn Mater* 449:385–389
- [17] Guo XW, Liu P, Han JH, Ito Y, Horata A, Fujuta T, Chen MW (2015) 3D nanoporous nitrogen-doped graphene with encapsulated RuO₂ nanoparticles for Li-O₂ batteries. *Adv Mater* 27:6137–6143
- [18] Lv HL, Ji GB, Liu W, Zhang HQ, Du YW (2015) Achieving hierarchical hollow Carbon@Fe@Fe₃O₄ nanospheres with superior microwave absorption properties and lightweight features. *J Mater Chem C* 3:10232–10241
- [19] Matsumoto M, Saito Y, Park C, Fykushima T, Aidal T (2015) Ultrahigh-throughput exfoliation of graphite into pristine ‘single-layer’ graphene using microwaves and molecularly engineered ionic liquids. *Nat Chem* 7:730–736
- [20] Xu HL, Yin XW, Li MH, Han MK, Hou ZX, Li XL, Zhang LT, Cheng LF (2018) Mesoporous carbon hollow microspheres with red blood cell like morphology for efficient microwave absorption at elevated temperature. *Carbon* 132:343–351
- [21] Wang C, Han X, Zhang X, Hu S, Zhang T, Wang J, Du Y, Wang X (2010) Controlled synthesis and morphology-dependent electromagnetic properties of hierarchical cobalt assemblies. *J Phys Chem C* 114:14826–14830
- [22] Wei B, Zhou JT, Yao ZJ, Haidry AA, Guo XL, Lin HY, Qian K, Chen WJ (2020) The effect of Ag nanoparticles content on dielectric and microwave absorption properties of β-SiC. *Ceram Int* 46:5788–5798
- [23] Lv HL, Gui YH, Yang ZH, Cheng Y, Wang LYP, Zhang BS, Zhao Y, Xu JZC, Ji GB (2017) A Brief Introduction to the fabrication and synthesis of graphene based composites for the realization of electromagnetic absorption materials. *J Mater Chem C* 5:491–512
- [24] Deng JS, Wang QB, Zhou YY, Zhao B, Zhang R (2017) Facile Design of a ZnO nanorod-Ni core-shell composite with dual peaks to tune its microwave absorption properties. *RSC Adv* 15:9294–9302
- [25] Liu P, Yao Z, Zhou J, Yang Z, Kong LB (2016) Small magnetic Co-doped NiZn ferrite/graphene nanocomposites and their dual-region microwave absorption performance. *J Mater Chem C* 4:9738–9749
- [26] Frenkel J, Dorfman J (1930) Spontaneous and induced magnetisation in ferromagnetic bodies. *Nature* 126:274–275
- [27] Wang H, Meng F, Huang F, Jing C, Li Y, Wei W (2019) Interface modulating cnts@pani hybrids by controlled

- unzipping of the walls of cnts to achieve tunable high-performance microwave absorption. *ACS Appl Mater Iner* 11:12142–12153
- [28] Wei B, Zhou JT, Yao ZJ, Haidry AA, Qian K, Lin HY, Guo XL, Chen WJ (2020) Excellent microwave absorption property of nano-Ni coated hollow silicon carbide core-shell spheres. *Appl Surf Sci* 508:145261
- [29] Lei YM, Yao ZJ, Lin HY, Zhou JT, Haidry AA, Liu PJ (2018) The effect of polymerization temperature and reaction time on microwave absorption properties of Co-doped ZnNi ferrite/polyaniline composites. *RCS Adv* 8:29344–29355
- [30] Lv HL, Ji GB, Liang XH, Zhang HQ, Du YW (2015) A novel rod-like $\text{MnO}_2@Fe$ loading on graphene giving excellent electromagnetic absorption properties. *J Mater Chem C* 3:5056–5064
- [31] Qian K, Yao ZJ, Lin HY, Zhou JT, Haidry AA, Qi TBH, Chen WJ, Guo XL (2020) The influence of Nd substitution in Ni-Zn ferrites for the improved microwave absorption properties. *Ceram Int* 46:227–235
- [32] Wang Z, Wu L, Zhou J, Jiang Z, Shen B (2014) Chemoselectivity-induced multiple interfaces in MWCNT/ $\text{Fe}_3\text{O}_4@ZnO$ heterotrimers for whole X-band microwave absorption. *Nanoscale* 6:12298–12302
- [33] Wang S, Huang F, Zhang M, Kong X, Zi Z, Liu Q (2018) Fe_3O_4 /carbon chain-like core/shell composites: Synthesis and microwave absorption properties. *Integr Ferroelectr* 190:76–84
- [34] Li C, Ge Y, Jiang X, Waterhouse GI, Zhang Z, Yu L (2018) Porous $\text{Fe}_3\text{O}_4/C$ microspheres for efficient broadband electromagnetic wave absorption. *Ceram Int* 44:19171–19183
- [35] Zeng Q, Xu D, Chen P, Yu Q, Xiong X, Chu H, Wang Q (2018) 3D graphene-Ni microspheres with excellent microwave absorption and corrosion resistance properties. *J Mater Sci-Mater El* 29:2421–2433

Publisher's Note Springer Nature remains neutral with regard to jurisdictional claims in published maps and institutional affiliations.